Submitted to Energy Conversion and Management

Type of contribution: Full-length article (Accepted manuscript)

Control structure design of a solid oxide fuel cell and molten carbonate fuel cell integrated system: Bottom-up analysis

Prathak Jienkulsawad[a], Sigurd Skogestad[b], and Amornchai Arpornwichanop[a,c*]

[a] Center of Excellence in Process and Energy Systems Engineering, Department of Chemical Engineering, Faculty of Engineering, Chulalongkorn University, Bangkok 10330, Thailand

[b] Department of Chemical Engineering, Norwegian University of Science and Technology, N-7491 Trondheim, Norway

[c] Chemical Engineering Research Center for Bio-, Circular-, and Green-Economy, Faculty of Engineering, Chulalongkorn University, Bangkok 10330, Thailand

[*]E-mail address: Amornchai.a@chula.ac.th.

Abstract

A solid oxide fuel cell and molten carbonate fuel cell integrated system is a power generation system with enhanced fuel and carbon dioxide utilization. Due to its complex structure, designing a control system is important for its smooth and efficient operation. This study is a continuation from the previous study focusing on a top-down, steady-state economic analysis for synthesizing the control structure of the solid oxide fuel cell and molten carbonate fuel cell integrated system to maximize power generation and carbon dioxide utilization. In this study, a bottom-up analysis is further performed to design a control layer of such a fuel cell integrated system and validate the proposed control structure via dynamic simulation. The control configuration using a decentralized approach with proportional-integral-derivative control is considered to maintain the fuel cell system at its optimum target. The control performance with the proposed control structure and configurations are evaluated and analyzed. Four control loops involving gas concentrations are considered, based on different time scales between the regulatory control and supervisory layers. The results of the proposed control system confirm that the integrated fuel cell system is controllable despite the deviation of the fuel cell voltages from their nominal values.

Keywords: Solid oxide fuel cell; Molten carbonate fuel cell; Integrated system; Control structure design; Bottom-up analysis

1. Introduction

Solid oxide fuel cell (SOFC) is considered alternative, reliable power device to replace combustion-based power generators [1]. It provides higher energy conversion efficiency, lower environmental impact, adequate fuel flexibility, and the possibility for combined heat and power generation with a wide range of applications [2]. For small applications, a SOFC system combined with adsorption and hybrid chillers was applied to a telecommunication system providing the electrical (<10 kW) and cooling (<20 kW) energy to a base transceiver station and data center, and can save energy about 110 MWh per year compared to a traditional system [3]. The SOFC can also be possibly used as a power generation in the trigeneration system for an educational building with 900 m^2 and 120 kW requirement, giving the overall efficiency of 60% [4]. In addition, the SOFC can act as a fuel reforming when it is in the upstream process with a direct natural gas fuel feed. The reformed gas from the SOFC can further used in the downstream process of power generation, which can improve the overall energy efficiency by 16% when integrated with a proton exchange membrane fuel cell (PEMFC) [5]. The SOFC system integrated with a solid oxide electrolyser was employed in the industrial facilities of the paper mill and can enhance energy generation efficiency by 6% [6]. Besides stationary applications, SOFCs can be used in a transportation sector. Bessekon et al. [7] showed that a driving range of the SOFC-battery electrical vehicle using a Nissan Leaf Acenta module fed by compressed natural gas, liquefied natural gas, and liquefied petroleum gas can be enhanced by 94 km, 535 km and 653 km, respectively, compared to the original electrical vehicle [7].

Regarding the power generation system, there are many possible integrated systems with SOFCs. For example, a SOFC integrated with a homogeneous charge compression ignition engine can enhance electrical efficiency to 59% [8], a SOFC integrated with a gas turbine (GT) and steam turbine has yielded a promising overall energy efficiency of 66.8%

[9], and a SOFC integrated with a PEMFC with the gas processing subsystem consisting of a water gas shift reactor and thermal swing adsorption has provided an overall energy efficiency of 64% [10]. Integrated systems are of interest as fuel cannot be used fully by the SOFC itself and can be used for additional power or heat generation. Jienkulsawad et al. [11] proposed the integration of two high-temperature fuel cells, SOFC and MCFC, to enhance fuel and carbon dioxide utilization, providing an electrical efficiency of 57.1%. By integrating SOFC with MCFC, the nickel oxide (NiO) formation on the anode of the SOFC [12], decreasing the catalytic activity due to hydrogen deficiency, can be avoided [13]. The formation of NiO also causes a microstructural change, resulting in long-term cell degradation [14].

In general, the integration of the fuel cells leads to a complicated system involving many controlled and manipulated variables. Thus, the control design of integrated fuel cell systems is essential for efficient operation. There are many possible control structures for fuel cell systems. Xue et al. [15] successfully used a fuzzy fault-tolerance controller coupled with a Bayesian regularization neural network to control a SOFC with a reformer system; the SOFC system could be operated safely despite fluctuations in the steam feed flow rate. A linear-quadratic-Gaussian control was used to control a wind turbine-SOFC hybrid system, resulting in an increased system lifetime [16]. Chen et al. [17] implemented six control loops to ensure the safe and effective operation of a SOFC-GT hybrid system with anode and cathode recirculation, in which the gas feed temperatures to the anode and cathode were controlled to avoid significant temperature differences and temperature gradient in the SOFC. This finding was also observed by Jienkulsawad et al. for a SOFC-MCFC integrated system [18]. A plantwide control configuration with an internal model control-based multi-loop control was successfully used to control the SOFC-GT hybrid system to meet the complete combustion, high power, lowest heat loss, and carbon dioxide emissions requirements [19]. A

fuel cell system can be controlled to follow the load demand while achieving maximum efficiency point tracking by controlling the fuel consumption [20]. From literature reviews, most academic work has focused on stabilizing control and less on economic control. Regarding different system designs and control objectives, economic control of the integrated fuel cell system should be further considered while keeping its stabilization. The control structure design procedure of Skogestad [21] considers both of these issues. With such a control structure design, Chatrattanawet et al. [22] simulated an economic control scheme for a standalone SOFC system. Jienkulsawad et al. [18] performed a top-down analysis, the first half part of the control structure design procedure, of the integrated SOFC-MCFC system. The economic objective was to minimize the power generation costs and penalty costs of carbon dioxide emission (carbon tax) subjects to satisfy operational conditions; the self-optimizing controlled variables and throughput manipulator (TPM) were selected. Although suitable controlled variables from an economic point of view were identified in the previous work, a bottom-up analysis, the second part of the control structure design procedure, is necessary to validate whether the designed control structure can be efficiently implemented in practice.

The present work focuses on the bottom-up part of the plantwide control procedure, including the selection of manipulated variable (MV)-controlled variable (CV) pairings and the control configuration. The relative gain array (RGA) is used as a tool for selecting input-output pairings for decentralized control. Finally, the proposed control system is validated via dynamic simulations using Matlab.

2. Process description and models

A series configuration of the integrated SOFC-MCFC system is considered as shown in Figure 1. Methane (CH_4) and steam (H_2O) are fed as a hydrogen source to the reformer

where the synthesis gas (e.g., carbon monoxide (CO), hydrogen (H_2), and carbon dioxide (CO_2)) generation takes place according to reactions (i) and (ii) in Table 1. A steam to methane molar feed ratio (S/C) of 2 is kept constant to avoid carbon formation in the SOFC [23] and the reformer operates at 1 atm and 973 K. The synthesis gas is introduced to the SOFC anode, whereas air is fed to the SOFC cathode and reacts via electrochemical reactions (iii)–(v) in Table 1. Additional electric power is generated in the MCFC via reactions (vi)–(viii). The feed temperatures of the SOFC and MCFC were in a range of 973–1073 K and 823–873 K, respectively. The MCFC anode off-gas containing the remaining CO and H_2 is mixed with part of the cathode off-gas and burned in a combustion chamber to generate additional energy and concentrate the CO_2 before it is recirculated back to the cathode of the MCFC.

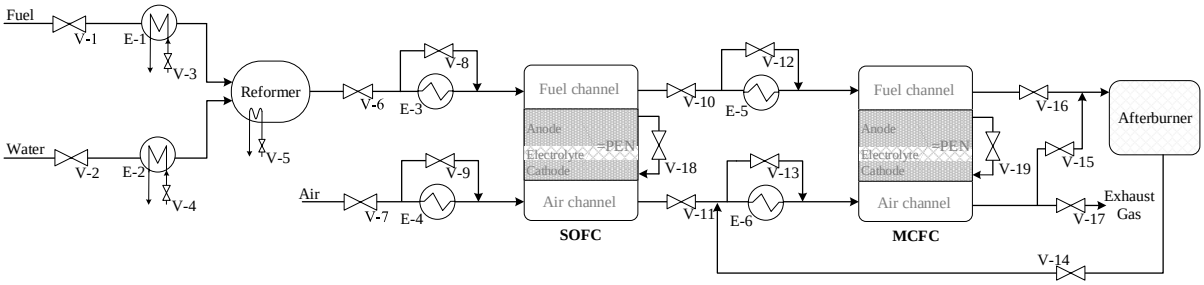

Fig. 1 Series configuration of the integrated SOFC-MCFC system.

Table 1. Chemical reactions

Reformer	SOFC	MCFC		
•	•	•	Steam reforming reaction (SR) $CH_4 + H_2O \leftrightarrow 3H_2 + CO$	(i)
•	•	•	Water-gas-shift reaction (WGS) $CO + H_2O \leftrightarrow H_2 + CO_2$	(ii)
	•		Oxidation reaction (anode) $H_2 + O^{2-} \rightarrow H_2O + 2e^-$	(iii)
	•		Reduction reaction (cathode) $0.5O_2 + 2e^- \rightarrow O^{2-}$	(iv)
	•		Overall electrochemical reaction $H_{2,(an)} + 0.5O_{2,(ca)} \rightarrow H_2O_{,(an)}$	(v)
		•	Oxidation reaction (anode) $H_2 + CO_3^{2-} \rightarrow H_2O + CO_2 + 2e^-$	(vi)
		•	Reduction reaction (cathode) $0.5O_2 + CO_2 + 2e^- \rightarrow CO_3^{2-}$	(vii)
		•	Overall electrochemical reaction $H_{2,(an)} + 0.5O_{2,(ca)} + CO_{2,(ca)} \rightarrow CO_{2,(an)} + H_2O_{,(an)}$	(viii)

The fuel cell mathematical model (Table 2) includes mass and energy balances, as well as electrochemical models. Due to the high temperature, the radiation heat between the Positive-electrode(cathode)/Electrolyte/Negative-electrode(anode) (PEN) structure and interconnect (for connecting the neighboring cell) is included. The power generated by the fuel cells can be computed from the electrochemical part of the model, which relates the gas composition and temperature to the cell voltage (E) and current density (j). The mathematical model is based on the following assumptions: (1) pressure drop inside the channels is

neglected, (2) heat loss to the surroundings is neglected, (3) all gases behave as ideal gases, (4) only hydrogen oxidation is considered, and (5) complete combustion in the afterburner. The fuel cell models were validated with the experimental data from the literature in our previous study at various operating temperatures [24]. The fuel cell dimensions and electrochemical parameters are given in Tables 3 and 4.

Table 2. Summary of fuel cell models [18]

Mass balances (fuel and air channel)

$$\left.\frac{dN_i}{dt}\right|_{i\in\{\text{gaseous species}\}} = F_{0i} - F_i + \sum_j \nu_{i,j}\hat{R}_j A \tag{1}$$

Energy balances

Fuel Channel: $$\rho_f Cp_f V_f \frac{dT_f}{dt} = H_{0f} - H_f + Q_{P,f} + Q_{I,f} + \sum_{j\in\{(i),(ii)\}} \left(-\Delta H\right)_j \hat{R}_j A \tag{2}$$

Air Channel: $$\rho_a Cp_a V_a \frac{dT_a}{dt} = H_{0a} - H_a + Q_{P,a} + Q_{I,a} \tag{3}$$

PEN: $$\rho_P Cp_P V_P \frac{dT_P}{dt} = -Q_{P,f} - Q_{P,a} + Q_{rad} - IE + \left(-\Delta H\right)_{(v)} \hat{R}_{(v)} A \tag{4}$$

Interconnect: $$\rho_I Cp_I V_I \frac{dT_I}{dt} = -Q_{I,f} - Q_{I,a} - Q_{rad} \tag{5}$$

Enthalpy flow in/out $$\underset{k\in\{0f,0a,f,a\}}{H_k} = \sum_i F_i \int_{298}^{T_k} Cp_i dT \tag{6}$$

Heat conduction: $$\underset{j\in\{P,I\},k\in\{f,a\}}{Q_{j,k}} = \frac{Ak_k Nu\left(T_j - T_k\right)}{D_h} \tag{7}$$

Heat radiation: $$Q_{rad} = A\left(\frac{\sigma\left(T_I^4 - T_P^4\right)}{1/\epsilon_I + 1/\epsilon_P - 1}\right) \tag{8}$$

Electrochemical models

Cell Voltage: $$E = E_{OCV} - \sum \eta_{\text{loss}} \tag{9}$$

Current: $$I = jA \tag{10}$$

Fuel Utilization: $$U_f = \frac{I}{2\mathbb{F}(4F_{\mathrm{CH_4}} + F_{\mathrm{CO}} + F_{\mathrm{H_2}})} \tag{11}$$

SOFC: Open-circuit voltage: $$E_{OCV,S} = E^0 - \frac{\Re T}{2\mathbb{F}} \ln\left(\frac{P_{\mathrm{H_2O}}}{P_{\mathrm{H_2}} P_{\mathrm{O_2}}^{0.5}}\right) \tag{12}$$

Concentration overpotentials:

$$\eta_{\mathrm{con}} = \frac{\Re T}{2\mathbb{F}} \ln\left(\frac{P_{\mathrm{H_2O},TPB} P_{\mathrm{H_2},f}}{P_{\mathrm{H_2O},f} P_{\mathrm{H_2},TPB}}\right) + \frac{\Re T}{4\mathbb{F}} \ln\left(\frac{P_{\mathrm{O_2},a}}{P_{\mathrm{O_2},TPB}}\right) \tag{13}$$

Activation overpotentials:

$$j = j_{0,an}\left[\frac{P_{\mathrm{H_2},TPB}}{P_{\mathrm{H_2},f}} \exp\left(\frac{\alpha n \mathbb{F}}{\Re T}\eta_{\mathrm{act},an}\right) - \frac{P_{\mathrm{H_2O},TPB}}{P_{\mathrm{H_2O},f}} \exp\left(-\frac{(1-\alpha) n \mathbb{F}}{\Re T}\eta_{\mathrm{act},an}\right)\right] \tag{14}$$

$$j = j_{0,ca}\left[\exp\left(\frac{\alpha n \mathbb{F}}{\Re T}\eta_{\mathrm{act},ca}\right) - \exp\left(-\frac{(1-\alpha) n \mathbb{F}}{\Re T}\eta_{\mathrm{act},ca}\right)\right] \tag{15}$$

Ohmic losses: $$\eta_{\mathrm{ohm}} = j\sum_i \frac{\tau_i}{\sigma_i} \tag{16}$$

MCFC: Open-circuit voltage: $$E_{OCV,M} = -\frac{\Delta G}{2\mathbb{F}} - \frac{\Re T}{2\mathbb{F}} \ln\left(\frac{P_{\mathrm{H_2O}} P_{\mathrm{CO_2},f}}{P_{\mathrm{H_2}} P_{\mathrm{O_2}}^{0.5} P_{\mathrm{CO_2},a}}\right) \tag{17}$$

Total losses: $$\sum \eta_{\mathrm{loss}} = \left(R_{ir} + R_{an} + R_{ca}\right) j \tag{18}$$

Anode resistance: $$R_{an} = 2.04\times10^{-3} \exp\left(\frac{23.7}{\Re T}\right) P_{\mathrm{H_2}}^{-0.5} \tag{19}$$

Cathode resistance:

$$\begin{aligned} R_{ca} = {} & 3.28\times10^{-9} \exp\left(\frac{132}{\Re T}\right) P_{\mathrm{O_2}}^{-0.75} P_{\mathrm{CO_2}}^{0.5} \\ & + 3.39\times10^{-6} \exp\left(\frac{67.1}{\Re T}\right)\left(2\times10^{-5} y_{\mathrm{H_2O}} + y_{\mathrm{CO_2}}\right)^{-1} \end{aligned} \tag{20}$$

Electrolyte resistance: $R_{ir} = 1.12 \times 10^{-2} \exp\left(\frac{23}{\Re T}\right)$ (21)

Table 3. Fuel cell dimensions [24]

	SOFC	**MCFC**
Cell length, L (m)	0.4	0.4
Cell width, W (m)	0.1	0.8
Fuel channel height, h_f (mm)	1	0.8
Air channel height, h_a (mm)	1	0.8
Anode thickness, τ_{an} (μm)	500	-
Cathode thickness, τ_{ca} (μm)	50	-
Electrolyte thickness, τ_{el} (μm)	20	-
PEN thickness, τ_{PEN} (μm)	570	1000

Table 4. Electrochemical parameters [24]

α (–)	0.5
σ_{an} ($\mathrm{ohm^{-1}m^{-1}}$)	$(9.5\times10^{7}/T)\exp(-1150/T)$
σ_{ca} ($\mathrm{ohm^{-1}m^{-1}}$)	$(4.2\times10^{7}/T)\exp(-1200/T)$
σ_{el} ($\mathrm{ohm^{-1}m^{-1}}$)	$33.4\times10^{3}\exp(-10300/T)$
η_{DC-AC} (%)	94

3. Control structure design: Bottom-up analysis

The control structure design procedure of Skogestad [21] consists of two main parts; the top-down and the bottom-up part as outlined in Figure 2. The main result from the top-down part (steps S1 to S4) is the selection of controlled outputs, mainly based on an economic steady-state optimization. From the previous study on the top-down analysis of the integrated SOFC-MCFC system (Figure 1) [18], three active constraint regions (I, II, and III) as a function of the two main disturbances (fuel feed flowrate and steam feed flowrate) were identified. The normal operating point is in region I. Fortunately, the proposed set of eight controlled variables (CV1) in regions I and II are the same, as $\mathrm{CV1}=\left[T_{0f,S}, T_{0a,S}, y_{\mathrm{O}_2,M_{0a}}, y_{\mathrm{H}_2,M_f}, T_{0a,M}, T_{f,M}/T_{0f,M}, y_{\mathrm{H_2O},B_0}, U_{f,M}\right]$. Fuel utilization ($U_{f,M}$) is not an active constraint in region I but the loss is small while constant at 75%. This implies that regions I and II can use the same control structure (Control structure A in [18]). This choice for CV1 is infeasible for region III due to the insufficient steam that is supplied to the system. However, feasibility is achieved when hydrogen at the MCFC anode outlet (y_{H_2,M_f}) is replaced by hydrogen in the SOFC anode outlet (y_{H_2,S_f}); this choice gives the smallest economic loss in region III. The electric power output, or more precisely, the MCFC current (V-19 in Figure 1), was chosen as the throughput manipulator (TPM) because most of active constraints occur around the MCFC, indicating that it needs to be tightly controlled.

The bottom-up part (steps S5 to S7) deals with the design of the control system, including the selection of additional controlled outputs and pairings with manipulated inputs (valves V in Figure 1). More details are given in the following sections.

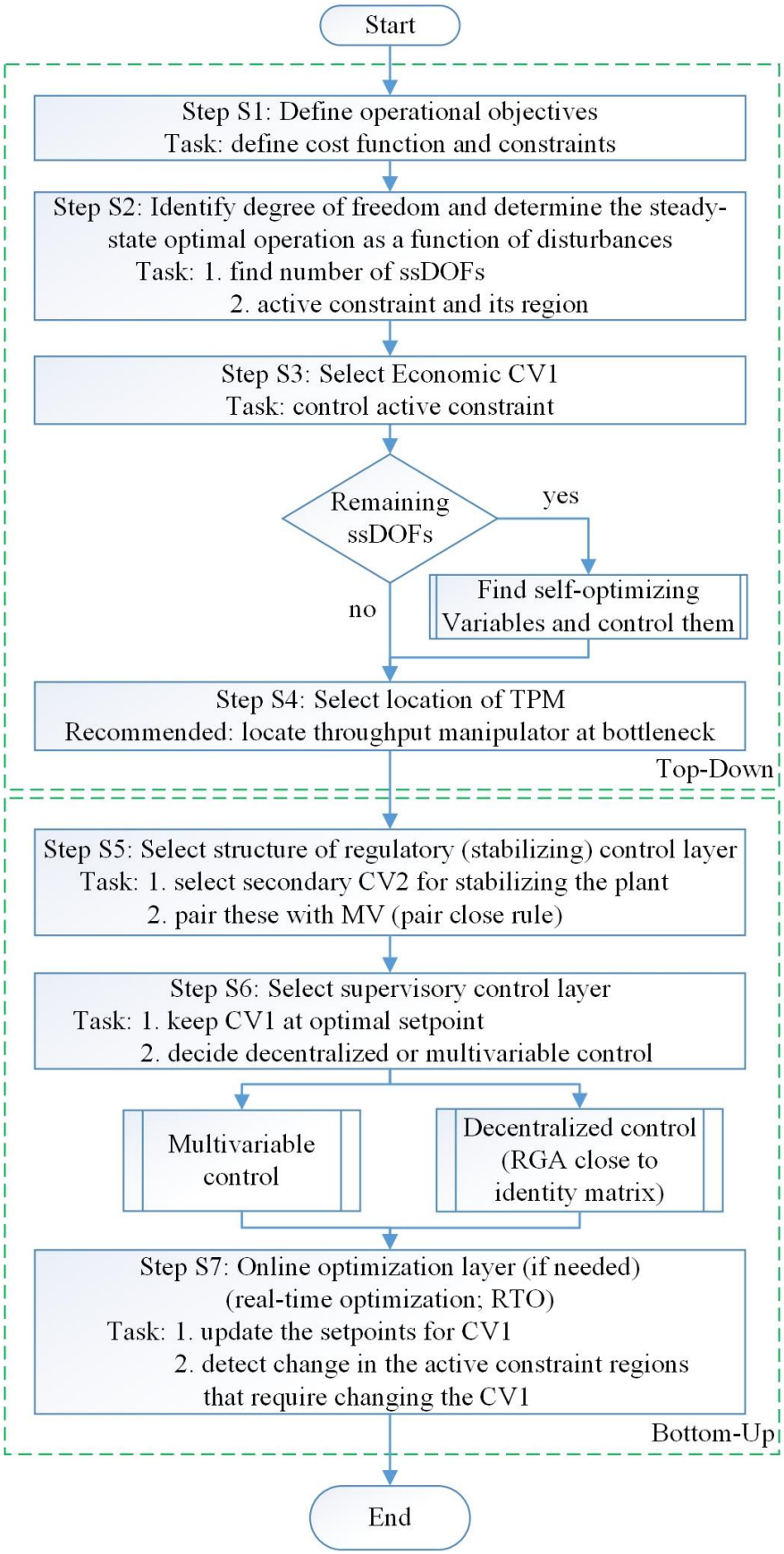

Fig. 2 Control structure design procedure.

3.1 Step S5. Structure of stabilizing control layer

The system should not drift too far from its acceptable operating point so as to ensure safe and stable operation. Among the 19 manipulated inputs (V1–V19 shown in Figure 1), 8 inputs are used to control the economically controlled variables (CV1) found in the top-down part [18]. In addition, the MCFC current (V-19) is chosen as the TPM. The 10 remaining inputs are used to control 10 specified variables (CV2), including the steam to carbon ratio, temperatures, and pressures. Specifically, the set CV2 in this study is:

$$\mathrm{CV2} = \left[S/C, T^{0}_{\mathrm{CH_4}}, T^{0}_{\mathrm{H_2O}}, T_R, P_R, P_{f,S}, P_{a,S}, P_{f,M}, P_{a,M}, P_B \right]$$

The steam to carbon ratio (S/C) is controlled to avoid carbon formation in the SOFC. The temperatures are controlled to achieve the design conditions and avoid material stress in the fuel cells. The fuel cell voltage is also an important parameter but it is given indirectly from the hydrogen concentration and cell temperatures as reported in Chatrattanawet et al. (2015) [22]. The pressures represent gas holdups (inventory) and need to be controlled to achieve stable operation. The pairing of the pressure inventory loops follows the radiation rule [25] with the TPM located at the MCFC current (V-19).

Note that to simplify the model, the dynamics of these 10 loops are not included in the dynamic model, assuming adequate control in all pressure loops and considering all units are running at a static pressure of 1 atm. Rather, these ten variables are specified in the model equations, which are all assumed to be static except for the fuel cell models (Table 2).

At this point, it is necessary to discuss the (dynamic) controllability of the system. To this effect, the locations of the poles and zeros are shown in Fig. 3. The poles and zeros are independent of the controller and control configuration and, therefore, reflect the controllability of the plant. Poles can tell whether the system is stable or not, whereas the zeros have an impact on the system's transient characteristics. Unstable (RHP) zeros can

imply serious control problems. Figure 3 shows that all poles and zeros are stable (in LHP), so no particular problem is foreseen.

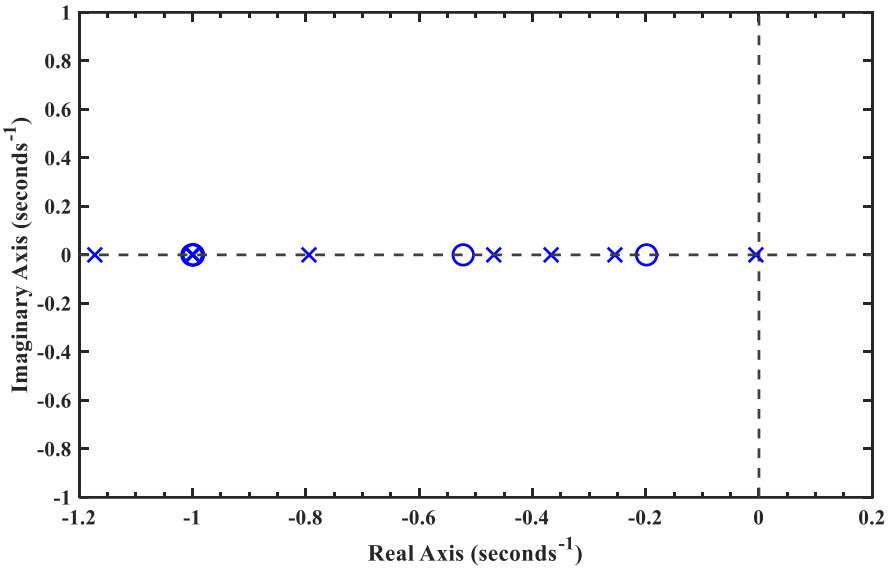

Fig. 3 Pole (x) and Zero (o) map of the dynamic model of the integrated system. There is an additional stable pole located at -11.2 s^{-1}.

3.2 Step 6. Select supervisory control layer.

In this step, controllers are implemented to keep the eight economic controlled variables (CV1) at their optimal setpoints. Proportional-integral-derivative (PID) controllers are employed because they are common in industry, simple, cheap, and easy to implement. The control structure covering the normal operation (region I and II) is considered in this paper. Region III is considered the abnormal operation, happening when the fuel cell system has to increase the fuel feed and decrease the steam feed to reach the higher power demand without energy efficiency concerns. To avoid having the system cross to region III, a ratio controller is used to adjust the steam feed according to the methane feed (for controlling S/C in CV2). In total, with the TPM located at V-19, 18 outputs (8 in CV1 and 10 in CV2) need to be controlled; therefore, identifying 18 pairings is required. The number of possible pairing combinations is very large (18! = 6.4e^{15}). Fortunately, most of the pairings are obvious and

can be decided by the "pair-close" rule (Rule 9 of Minasidis et al. [26]) and by the radiation rule around the TPM. For example, the temperatures on the six heat exchangers should be controlled by their respective bypass flows [27]. This removes pairing choices from the four temperatures in the CV1 set. The following choice of pairings for the remaining four outputs in CV1 is considered.

$$\mathrm{CV1}_C = \left[y_{\mathrm{O}_2,M_{0a}}, y_{\mathrm{H_2O},B_0}, U_{f,M}, y_{\mathrm{H}_2,M_f} \right]$$

These four variables involve composition measurements and are controlled on a relatively slow time scale so interactions between the loops can be significantly large. The other 14 variables are expected to be controlled locally on a fast time scale, so interactions will be much less. They are, in this analysis, assumed to be perfectly controlled, so pairing selection is not relevant. To control the four compositions in $\mathrm{CV1_C}$, there are several choices for manipulated inputs. $y_{\mathrm{O}_2,M_{0a}}$ can be either controlled by valve (V-7) or V-11. $y_{\mathrm{H_2O},B_0}$ can be either controlled by V-15 or V-16. y_{H_2,M_f} can be either controlled by V-10 or V-18. The fuel utilization $U_{f,M}$ is a function of the SOFC current density (V-18) and MCFC fuel feed (V-10), so it can be controlled by V-10 or V-18. Therefore, there are 6 possible MVs (V-6, V-7, V-10, V-11, V-15, and V-18) to control the four outputs in $\mathrm{CV1_C}$. However, only the four combinations in Tables 5–8 need to be considered: V-15 and V-18 appear in all sets because they are needed to control either $y_{\mathrm{H_2O},B_0}$, $U_{f,M}$, or y_{H_2,M_f}. V-6 and V-10 cannot appear in the same MV set because one of them is needed for pressure control. This argument also applies for V-7 and V-11.

As single-loop controllers (decentralized control) are implemented, input-output pairings are necessary; for this, the relative gain array (RGA) is a useful tool. The RGA of a non-singular square complex matrix (G) is given in Eq. (22), where × denotes element by element multiplication.

$$\mathrm{RGA}(G) = \Lambda(G) = G \times \left(G^{-1}\right)^{T} \tag{22}$$

The steady-state RGA is shown for the four alternative MV sets in Tables 5 to 8. The main rule when using the steady-state RGA is to avoid pairing on negative RGA-elements otherwise, the use of integral action adds instability if one of the loops is no longer active; for example, due to MV saturation. Based on this rule, there is only one possible pairing choice (shown in boldface) for each of the four MV sets.

In addition to avoiding negative RGA-elements, the value of the RGA-elements close to 1 is preferred for the selected pairings and with the other RGA-elements close to 0. From this reasoning, MV set 2 in Table 6 comes out as the preferred choice with all paired RGA-elements close to 1. The resulting choice of pairings is then as follow for the set $CV1_C$: V-7 controls $y_{O_2,M_{0a}}$, V-15 controls y_{H_2O,B_0}, V-10 controls $U_{f,M}$, and V-18 controls y_{H_2,M_f}. This means that V-6 and V-11 will be used to control pressures in the fuel channel and air channel of the SOFC, respectively. The proposed pairings for all the 18 loops are shown in Figure 4. The control loops in grey are for the set CV2. The control loops in red are the four temperature loops in $CV1_T$. Finally, the four control loops in blue are for remaining composition variables $CV1_C$. Note that in the simulations, controllers for these last four loops are only used. The remaining 14 variables are assumed to be perfectly controlled, which means that the pairings indicated are not really implemented in the present simulations. This is reasonable since these 14 loops are expected to be much faster than the four loops for $CV1_C$.

Table 5. RGA for $CV1_C$: MV set 1

	$F_{0f,S}$ (V-6)	$F_{0a,S}$ (V-7)	$F_{0a,B}$ (V-15)	I_S (V-18)
$y_{O_2,M_{0a}}$	0.0077	**0.9960**	-0.0040	0.0002
y_{H_2O,B_0}	-0.0187	-0.0022	**1.0045**	0.0164
$U_{f,M}$	-4.3249	-0.0372	0.0000	**5.3621**
y_{H_2,M_f}	**5.3359**	0.0433	-0.0005	-4.3787

Table 6. RGA for $CV1_C$: MV set 2

	$F_{0a,S}$ (V-7)	$F_{0f,M}$ (V-10)	$F_{0a,B}$ (V-15)	I_S (V-18)
$y_{O_2,M_{0a}}$	**1.0030**	-0.0002	-0.0041	0.0013
y_{H_2O,B_0}	-0.0036	-0.0038	**1.0121**	-0.0046
$U_{f,M}$	0.0012	**1.0987**	0.0000	-0.0999
y_{H_2,M_f}	-0.0005	-0.0947	-0.0079	**1.1032**

Table 7. RGA for $CV1_C$: MV set 3

	$F_{0f,S}$ (V-6)	$F_{0a,M}$ (V-11)	$F_{0a,B}$ (V-15)	I_S (V-18)
$y_{O_2,M_{0a}}$	-0.1029	**0.7574**	0.3343	0.0112
y_{H_2O,B_0}	-0.0157	0.2061	**0.7956**	0.0140
$U_{f,M}$	-4.7440	0.0000	0.0000	**5.7440**
y_{H_2,M_f}	**5.8626**	0.0365	-0.1299	-4.7693

Table 8. RGA for $CV1_C$: MV set 4

	$F_{0f,M}$ (V-10)	$F_{0a,M}$ (V-11)	$F_{0a,B}$ (V-15)	I_S (V-18)
$y_{O_2,M_{0a}}$	0.0019	**0.6934**	0.3073	-0.0026
y_{H_2O,B_0}	-0.0029	0.3070	**0.6992**	-0.0032
$U_{f,M}$	**1.0957**	0.0000	0.0000	-0.0957
y_{H_2,M_f}	-0.0946	-0.0004	-0.0065	**1.1015**

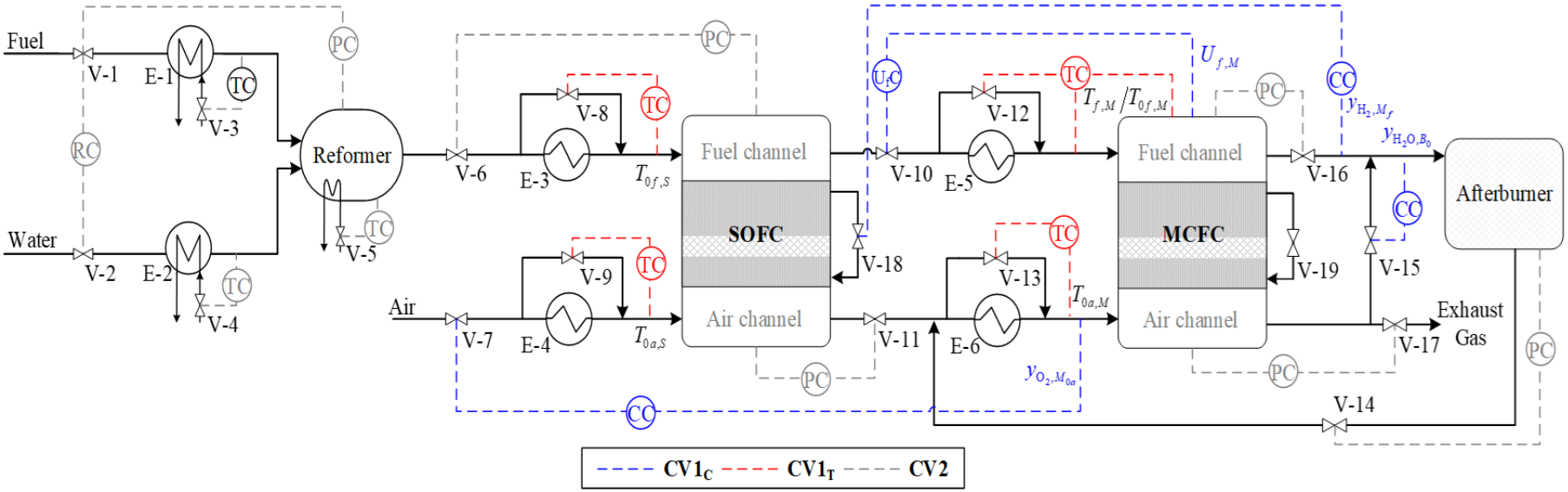

Fig. 4 Control structure A for regions I and II.

4. Simulation of closed-loop performance

To verify that the system is controllable using single-loop PID control, the system was simulated for setpoint changes (Figures 5–6) and disturbances in current (I_M) and feed rate (Figures 7–8). The controlled outputs are shown in Figures 5 and 7 and the manipulated inputs are shown in Figures 6 and 8. In addition, Figure 9 shows the resulting fuel cell voltages (E_S and E_M) for the case with disturbances. The dynamic responses are shown in Figures 5–9. The four PID controllers for controlling $y_{O_2,M_{0a}}$, y_{H_2O,B_0}, $U_{f,M}$, and y_{H_2,M_f} were tuned using the Skogestad internal model control (SIMC) tuning method, which is simple and works well on a wide range of processes [28]. To tune the controllers, a second-order model is first fitted for each of the four open-loops as:

$$g(s) = \frac{k}{(\tau_1 s + 1)(\tau_2 s + 1)} e^{-\theta s} \tag{23}$$

where k is the plant gain, θ is the effective time delay, τ_1 is the dominant lag time constant, and τ_2 is the second-order lag time constant. The SIMC settings for a cascade form PID controller are:

$$K_c = \frac{1}{k} \frac{\tau_1}{\tau_c + \theta} \tag{24}$$

$$\tau_I = \min\{\tau_1, 4(\tau_c + \theta)\} \tag{25}$$

$$\tau_D = \tau_2 \tag{26}$$

$$C_{PID}(s) = \frac{K_c(\tau_I s + 1)(\tau_D s + 1)}{\tau_I s} \tag{27}$$

where τ_c is the only tuning parameter. In this case, tight control is considered and thus, $\tau_c = \theta$ is selected. The resulting PID settings are given in Table 9.

To evaluate the closed-loop performance, an integral absolute error (IAE) of the control error ($e(t) = y_s - y(t)$) was determined; the IAE should be as small as possible.

$$\text{IAE} = \int_0^\infty |e(t)|\, dt \tag{28}$$

Table 9. PID controller parameters (cascade form)

	CV	K_c	τ_I	τ_D
1.	$y_{O_2,M_{0a}}$	0.09	2.61	0.18
2.	y_{H_2O,B_0}	-0.47	0.02	1.26
3.	$U_{f,M}$	-0.11	2.31	0.17
4.	y_{H_2,M_f}	-3.11E+05	3.91	1.52

4.1 Setpoint changes

As seen in Figure 5–6, all the dynamic responses are smooth according to the set-point changes shown in Table 10. Although the MV-CV pairings all have RGA-elements close to 1, there are some interactions. This is not surprising as, first, the RGA measures only two-way interactions and second, the RGA was obtained at steady-state conditions. Nevertheless, the interactions are quite small. At t_1, when the set point of $y_{O_2,M_{0a}}$ is increased, the first controller increases $F_{0a,S}$(V-7) as seen in Figures 5 and 6. However, because of the interaction, the second controller has to reduce $F_{0a,B}$(V-15) to keep y_{H_2O,B_0} constant. The main interaction is when a set-point change in $U_{f,M}$ alone is made in t_6 in Figures 5 and 6. This results in some interactions with the other loops as the MV used to control $U_{f,M}$, which is V-10 = $F_{0f,M}$, also affects the other CVs. Finally, note that at t_8 when the set-point of y_{H_2,M_f} is decreased by 10%, the fourth controller increases the SOFC current I_S(V-18). This

means that the SOFC anode-off gas will contain less fuel. This is akin to a reducing the fuel flow rate fed to MCFC resulting in the decrease of y_{H_2,M_f}.

Table 10. Timetable for set-point changes

Time (s)	Set-point change
$t_0 = 0$	Steady-state condition
$t_1 = 60$	$y_{\mathrm{O}_2,M_{0a}}$ is increased by 10%
$t_2 = 360$	$y_{\mathrm{O}_2,M_{0a}}$ is decreased by 10% from the original set-point
$t_3 = 660$	$y_{\mathrm{H_2O},B_0}$ is increased by 10% $y_{\mathrm{O}_2,M_{0a}}$ is changed back to its original
$t_4 = 960$	$y_{\mathrm{H_2O},B_0}$ is decreased by 10% from the original set-point
$t_5 = 1260$	$U_{f,M}$ is increased by 10% $y_{\mathrm{H_2O},B_0}$ is changed back to its original
$t_6 = 1560$	$U_{f,M}$ is decreased by 10% from the original set-point
$t_7 = 1860$	y_{H_2,M_f} is increased by 10% $U_{f,M}$ is changed back to its original
$t_8 = 2160$	y_{H_2,M_f} is decreased by 10% from the original set-point

4.2 Disturbance changes

The disturbance responses in Figures 7–9 are also smooth when the change is applied as seen in Table 11. Several remarkable observations on these responses can be made. At time t_1, when the MCFC power output (I_M) is increased by 10%, the MCFC needs more fuel to generate more power so both feed rates (V-7 and V-10) increase. This results in a

temporary drop in hydrogen at the MCFC anode outlet (y_{H_2,M_f}) and a rise in the stream mole fraction in the burner (y_{H_2O,B_0}). The oxygen at the MCFC cathode inlet ($y_{O_2,M_{0a}}$) is decreased initially because more O_2 is used in the power generation and burning. Hence, all the controllers act at the same time.

Table 11. Timetable for disturbances changes

Time (s)	Disturbance changes
$t_0 = 0$	Steady-state condition
$t_1 = 60$	MCFC current I_M (V-19) increased by 10%
$t_2 = 360$	MCFC current I_M (V-19) decreased by 10% from its original value
$t_3 = 660$	Methane feed flow rate (V-1) increased by 10% MCFC current I_M (V-19) shifted to its original value
$t_4 = 960$	Methane feed flow rate (V-1) decreased by 10% from its original value.
$t_5 = 1260$	Steam feed flow rate (V-2) increased by 10% Methane feed flow rate (V-1) shifted to its original value
$t_6 = 1560$	Steam feed flow rate (V-2) decreased by 10% from its original value

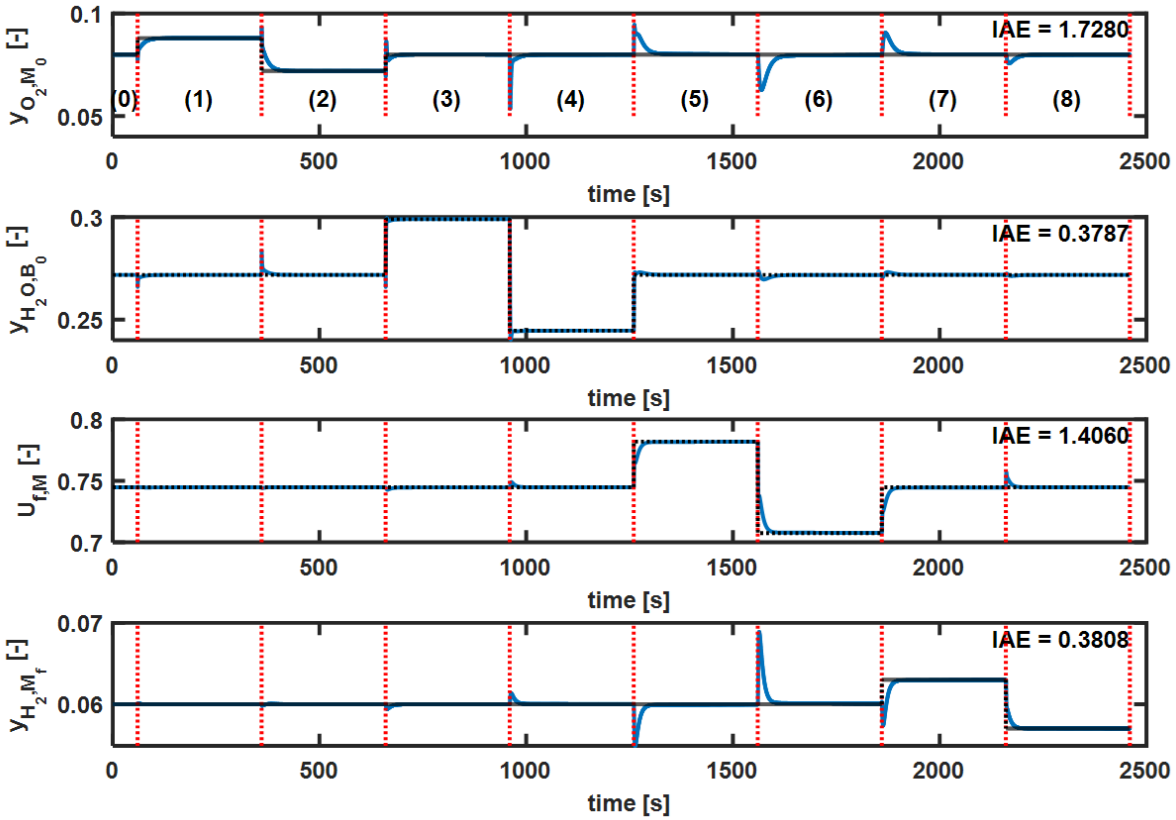

Fig. 5 Dynamic response of $CV1_C$ to set-point changes (Table 10).

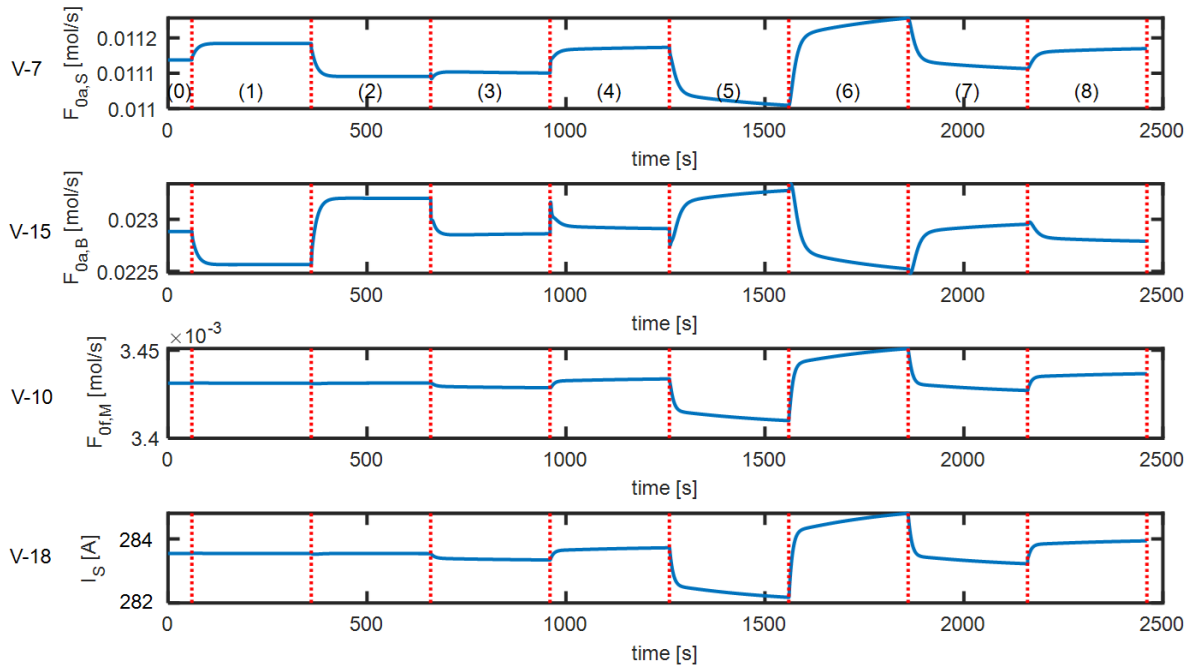

Fig. 6 Dynamic response of MVs to set-point changes (Table 10).

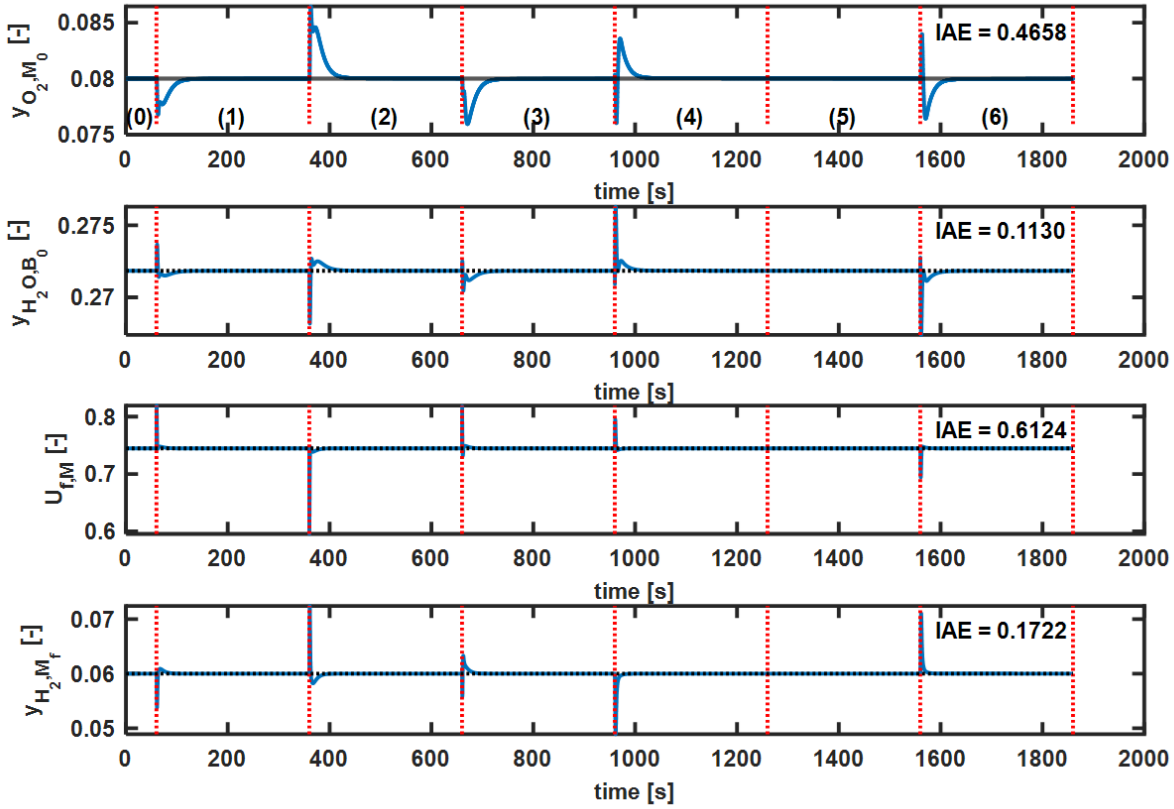

Fig. 7 Dynamic response of $CV1_C$ to disturbances (Table 11).

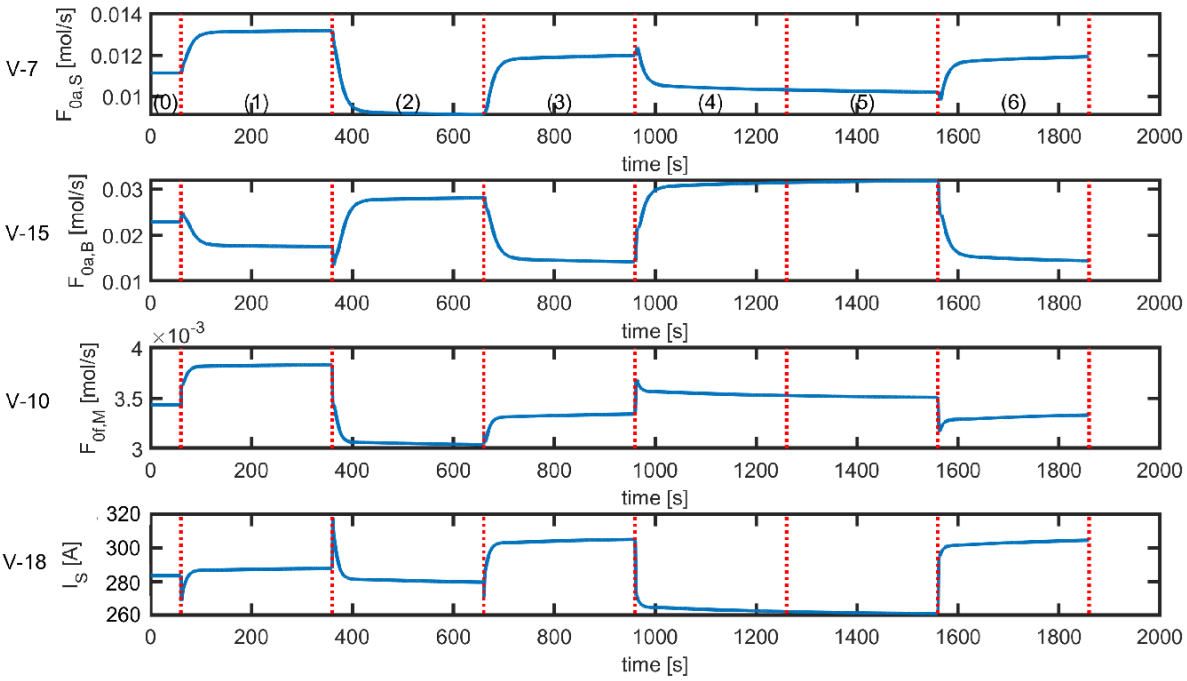

Fig. 8 Dynamic response of MVs to disturbances (Table 11).

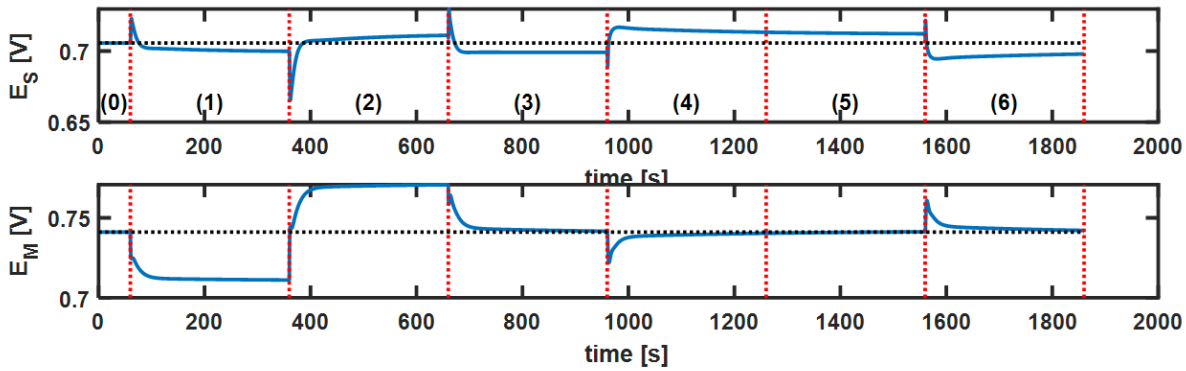

Fig. 9 Dynamic response of the uncontrolled fuel cell voltages to disturbances (Table 11).

The overall fuel cell system involves 18 control loops as shown in Figure 4. However, as already mentioned, the dynamic simulations only include the four slowest loops (in blue in Figure 4). The remaining 14 controlled outputs (CVs) are assumed as constant in the simulations (red and gray loops in Figure 4). The justification for this is the time scale separation, that is, that these 14 loops are assumed to be significantly faster and can be considered to be constant within the slower time scale of the 4 slower loops. This introduces a small error, but it also greatly simplifies the dynamic model and tuning. Note that the fuel cell system is modeled in MATLAB and part of the model is steady state. This makes it possible to directly specify output variables, like temperatures and pressures.

In comparison to other fuel cell control systems, the proposed control loops for the fuel cell system in this work are somewhat different from the control system proposed by other researchers [29]. Using the air flow rate is recommended to control the MCFC oxygen feed concentration instead of using it to control the temperature or fuel utilization. Similar to the work of Chatrattanawet et al. [22], control of the H_2 composition is essential to optimize economics. However, the following statement was found to not hold *"When the hydrogen concentration and temperature are controlled, voltage will be indirectly controlled"* [22]; the result of this study (Figure 9) shows that this is not true for this system. The cell voltages

cannot be controlled as they depend on the current, which is given by the operators and considered as a disturbance, and cell temperature. Although cell voltage cannot be controlled, it is still in the minimum allowance [30]. If the cell voltage needs to be controlled, for example if it drops too low, then the cell voltage would become the TPM. This should be easily implementable using a min-selector, for example.

5. Conclusions

In this work, the second part of a control structure based on Skogestad's procedure was performed for a SOFC-MCFC integrated system. In the first part, controlled variables were proposed to achieve close-to-optimal power generation while reducing carbon dioxide emissions and achieving safe operation [18]. In the second part, it was confirmed that this system is indeed controllable. The overall fuel cell system has 18 control loops (Figure 4) but because of the time scale separation between the regulatory layer and slower supervisory layer, only four slower composition loops were included in the dynamic simulation. The remaining 14 controlled outputs were assumed as constant in the simulation. RGA-analysis, used to select appropriate pairing of these four loops, and dynamic simulation of the fuel-cell system show that smooth responses can be achieved using simple single-loop PID controllers. The cell voltages deviated from their normal values, which were not controlled in our work.

Acknowledgments

The support of the Chulalongkorn Academic Advancement into its 2nd Century Project, and the Royal Golden Jubilee Ph.D. Program and Global Partnership Program (Thailand Science Research and Innovation) is gratefully acknowledged.

Nomenclature

Symbols

A	Area of reaction (m^2)
C_P	Heat capacity (J mol^{-1} K^{-1}, kJ kg^{-1} K^{-1})
CEC	Carbon emission coefficient ($kg\ CO_2\ MWh^{-1}$)
D_h	Hydraulic diameter (m)
E	Operating voltage (V)
E_{OCV}	Open-circuit voltage (OCV) (V)
E^0	OCV at standard temperature and pressure (V)
F_i	Mole flow rate (mol s^{-1})
$\mathbb{F}$	Faraday's constant (C mol^{-1})
H	Enthalpy flow (kW)
I	Current (A)
j	Current density (A m^{-2})
j_0	Exchange-current density (A m^{-2})
k	Thermal conductivity (kW m^{-1} K^{-1})
$\dot{m}$	Mass flow rate (mol s^{-1})
N_i	Mole of component *i* (mol)
Nu	Nusselt number (-)
P_i	Pressure (atm)
P_W	Power (W)

Greek symbols

α	transfer coefficient (-)
$\in$	emissivity (-)
η	voltage loss (V)
θ	time delay
$\Re$	Gas constant (kJ mol^{-1} K^{-1})
σ	Stefan-Boltzmann constant (W m^{-2} K^{-4})
σ_i	Electronical conductivity (ohm^{-1} m^{-1})
τ_1	time constant
τ_2	second-order lag time constant
τ_i	Thickness of layer *i* (m)

Subscripts

a	Air channel
an	Anode
B	Afterburner
ca	Cathode
el	Electrolyte
f	Fuel channel
I	Interconnect
i	Gas species
M	MCFC
P	PEN

Q	Heat (kW)	R	Reformer
$\hat{R}$	Rate of reaction per area (mol m^{-2} s^{-1})	S	SOFC
R	Rate of reaction (mol s^{-1})	TPB	Three-phase boundaries
T	Temperature (K)	0	Inlet
U_f	fuel utilization (%)	**Superscripts**	
V	Volume (m^3)	SP	Setpoint
y_i	Molar fraction (-)		

References

[1] J. Kupecki, M. Skrzypkiewicz, K. Motylinski, Variant analysis of the efficiency of industrial scale power station based on DC-SOFCs and DC-MCFCs, Energy 156 (2018) 292 - 298.

[2] M.E. Chelmehsara, J. Mahmoudimehr, Techno-economic comparison of anode-supported, cathode-supported, and electrolyte-supported SOFCs, International Journal of Hydrogen Energy 43 (2018) 15521 - 15530.

[3] V. Palomba, M. Ferraro, A. Frazzica, S. Vasta, F. Sergi, V. Antonucci, Experimental and numerical analysis of a SOFC-CHP system with adsorption and hybrid chillers for telecommunication applications, Applied Energy 216 (2018) 620-633.

[4] M. Mehrpooya, M. Sadeghzadeh, A. Rahimi, M. Pouriman, Technical performance analysis of a combined cooling heating and power (CCHP) system based on solid oxide fuel cell (SOFC) technology – A building application, Energy Conversion and Management 198 (2019) 111767.

[5] Z. Wu, P. Zhu, J. Yao, P. Tan, H. Xu, B. Chen, F. Yang, Z. Zhang, M. Ni, Thermo-economic modeling and analysis of an NG-fueled SOFC-WGS-TSA-PEMFC hybrid

energy conversion system for stationary electricity power generation, Energy 192 (2020) 116613.

[6] G. Vialetto, M. Noro, P. Colbertaldo, M. Rokni, Enhancement of energy generation efficiency in industrial facilities by SOFC – SOEC systems with additional hydrogen production, International Journal of Hydrogen Energy 44 (2019) 9608-9620.

[7] Y. Bessekon, P. Zielke, A. C. Wulff, A. Hagen, Simulation of a SOFC/Battery powered vehicle, International Journal of Hydrogen Energy 44 (2019) 1905-1918.

[8] Z. Wu, P. Tan, P. Zhu, W. Cai, B. Chen, F. Yang, Z. Zhang, E. Porpatham, M. Ni, Performance analysis of a novel SOFC-HCCI engine hybrid system coupled with metal hydride reactor for H_2 addition by waste heat recovery, Energy Conversion and Management 191 (2019) 119-131.

[9] M.A. Ehyaei, M.A. Rosen, Optimization of a triple cycle based on a solid oxide fuel cell and gas and steam cycles with a multiobjective genetic algorithm and energy, exergy and economic analyses, Energy Conversion and Management 180 (2019) 689-708.

[10] Z. Wu, M. Ni, P. Zhu, Z. Zhang, Dynamic modeling of a NG-fueled SOFC-PEMFC hybrid system coupled with TSA process for fuel cell vehicle, Energy Procedia 158 (2019) 2215-2224.

[11] P. Jienkulsawad, D. Saebea, Y. Patcharavorachot, A. Arpornwichanop, Performance assessment of a hybrid solid oxide and molten carbonate fuel cell system with compressed air energy storage under different power demands, International Journal of Hydrogen Energy 45 (2020) 835-848.

[12] P. Nehter, A high fuel utilizing solid oxide fuel cell cycle with regard to the formation of nickel oxide and power density, Journal of Power Sources 164 (2007) 252 - 259.

[13] P. Jienkulsawad, D. Saebea, Y. Patcharavorachot, S. Kheawhom, A. Arpornwichanop, Analysis of a solid oxide fuel cell and a molten carbonate fuel cell integrated system

with different configurations, International Journal of Hydrogen Energy 43 (2018) 932-942.

[14] T. Parhizkar, R. Roshandel, Long term performance degradation analysis and optimization of anode supported solid oxide fuel cell stacks, Energy Conversion and Management 133 (2017) 20 - 30.

[15] T. Xue, X. Wu, D. Zhao, Y. Xu, J. Jiang, Z. Deng, X. Fu, X. Li, Fault-tolerant control for steam fluctuation in SOFC system with reforming units, International Journal of Hydrogen Energy 44 (2019) 23360-23376.

[16] D. Yu, Y. Mao, B. Gu, S. Nojavan, K. Jermsittiparsert, M. Nasseri, A new LQG optimal control strategy applied on a hybrid wind turbine/solid oxide fuel cell/ in the presence of the interval uncertainties, Sustainable Energy, Grids and Networks 21 (2020) 100296.

[17] J. Chen, M. Liang, H. Zhang, S. Weng, Study on control strategy for a SOFC-GT hybrid system with anode and cathode recirculation loops, International Journal of Hydrogen Energy 42 (2017) 29422-29432.

[18] P. Jienkulsawad, S. Skogestad, A. Arpornwichanop, Control structure design of a solid oxide fuel cell and a molten carbonate fuel cell integrated system: Top-down analysis, Energy Conversion and Management 152 (2017) 88-98.

[19] W. Wu, S.-A. Chen, J.-J. Hwang, F.-T. Hsu, Optimization and control of a stand-alone hybrid solid oxide fuel cells/gas turbine system coupled with dry reforming of methane, Journal of Process Control 54 (2017) 90-100.

[20] N. Bizon, M. Oproescu, M. Raceanu, Efficient energy control strategies for a Standalone Renewable/Fuel Cell Hybrid Power Source, Energy Conversion and Management 90 (2015) 93 - 110.

[21] S. Skogestad, Control structure design for complete chemical plants, Computers & Chemical Engineering 28 (2004) 219 - 234.

[22] N. Chatrattanawet, S. Skogestad, A. Arpornwichanop, Control structure design and dynamic modeling for a solid oxide fuel cell with direct internal reforming of methane, Chemical Engineering Research and Design 98 (2015) 202 - 211.

[23] T.A. Adams II, J. Nease, D. Tucker, P.I. Barton, Energy conversion with solid oxide fuel cell systems: a review of concepts and outlooks for the short- and long-term, Ind Eng Chem Res 52 (2013) 3089 - 111.

[24] P. Jienkulsawad, A. Arpornwichanop, Investigating the performance of a solid oxide fuel cell and a molten carbonate fuel cell combined system, Energy 107 (2016) 843 - 853.

[25] E.M.B. Aske, S. Skogestad, Consistent inventory control, Industrial and Engineering Chemistry Research 48 (2009) 10892 - 10902.

[26] V. Minasidis, S. Skogestad, N. Kaistha, Simple rules for economic plantwide control, Computer Aided Chemical Engineering 37 (2015) 101 - 108.

[27] M. Escobar, J.O. Trierweiler, Bypass Design for Control and Optimization of Heat Exchanger Networks, Computer Aided Chemical Engineering 27 (2009) 1665-1670.

[28] S. Skogestad, Simple analytic rules for model reduction and PID controller tuning, Journal of Process Control 13 (2003) 291-309.

[29] B. Huang, Y. Qi, M. Murshed, Solid oxide fuel cell: Perspective of dynamic modeling and control, Journal of Process Control 21 (2011) 1426 - 1437.

[30] P. Aguiar, C. Adjiman, N. Brandon, Anode-supported intermediate temperature direct internal reforming solid oxide fuel cell: II. Model-based dynamic performance and control, Journal of Power Sources 147 (2005) 136 – 147.